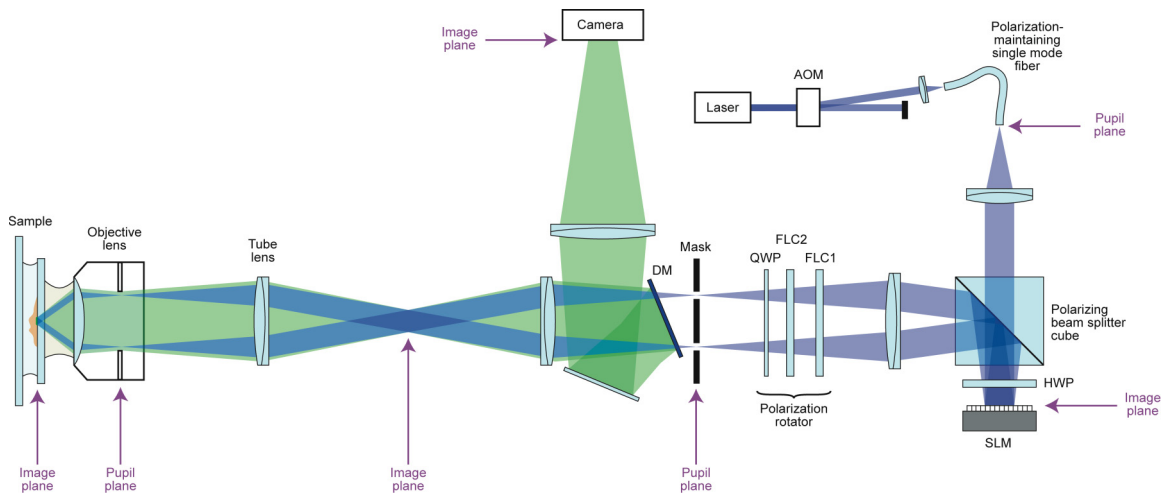**Supplementary Figure 1: Simplified diagram of the TIRF-SIM microscope**


Excitation light (488 nm, from an argon laser (Innova 90C, Coherent)) was coupled into a polarization-maintaining single-mode fiber (Oz Optics) after passing through an acousto-optic deflector (AOM-40 AF, Intra-Action) (here labeled AOM), which was used as a fast shutter and intensity control. Light exiting the fiber was collimated and sent through a pattern generator (described in **Supplementary Fig. 2**) consisting of a 1024 × 768 pixel ferroelectric-liquid-crystal-on-silicon spatial light modulator (Displaytech) (labeled SLM), a polarizing beam splitter cube, and a half-wave plate (labeled HWP). The light exiting the pattern generator was directed toward the microscope through a polarization rotator (described in **Supplementary Fig. 3**), consisting of two ferro-electric liquid crystal phase retarders (Displaytech) (labeled FLC1, FLC2) and a quarter wave plate (labeled QWP). A pupil-plane mask (labeled Mask) blocked unwanted diffraction orders caused by the finite-sized pixels of the SLM (**Supplementary Fig. 4**). The desired ±1 diffraction orders were refocused to points near opposite edges of the back focal plane of the microscope objective. Each beam was recollimated by the objective lens (100× / 1.49 TIRF, Nikon) and hit the cover slip surface at an angle that exceeded the critical angle for total internal reflection. Evanescent waves from the two beams extended ~100 nm into the specimen space and interfered there to produce a line pattern of excitation intensity. Fluorescent emission light (shown as green) from the specimen was directed toward a camera by a dichroic mirror as in a conventional fluorescence microscope.

**Supplementary Figure 2: Pattern generation with the SLM**
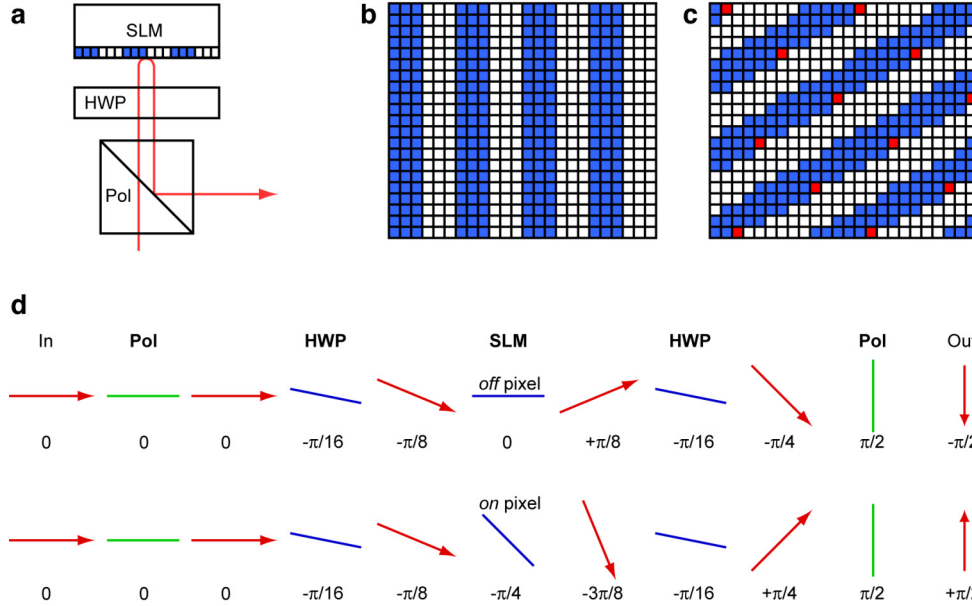
(**a**) The light path. Collimated, horizontally polarized light from the fiber traverses a polarizing beam splitter cube (labeled Pol) and a half-wave plate (HWP), is reflected by the SLM back through the half-wave plate, and its vertically polarized component is reflected by the cube and sent toward the objective. (**b–c**) SLM pixel patterns. The SLM consists of 1024x768 pixels, each of which can be digitally set to an *on* or an *off* state, which here produce 0 and π phase retardation of the light, respectively, at the output of the cube (see panel **d**). The choice of pattern had to satisfy several constraints. An efficient pattern for producing well-defined ±1 order diffraction components consist of parallel, equal-width alternating lines of 0 and π phase retardation. To be able to shift the phase of the pattern in steps of exactly $\pi/3$ (or $2\pi/3$), so as to generate the desired $2\pi/3$ phase shift between the +1 and -1 order beams, we wanted patterns with a horizontal or vertical period (in pixels) that is divisible by 3. For 2D SIM, we needed three patterns with similar line spacings but oriented at approximately 60° angle to each other. That the differently oriented patterns have near-identical line spacings is particularly important in TIRF SIM, because the line spacing dictates the beam separation in the pupil plane, which must fall within narrow tolerances in order to place all beams within the "TIRF ring," the narrow annulus between the edge of the pupil and the circle that corresponds to the critical angle (see **Supplementary Fig. 4**). Our chosen patterns for the 0° (panel **b**) and nominally 60° (panel **c**) orientations are shown with *off* and *on* pixels drawn in white and color respectively. The -60° pattern is identical to the +60° pattern except reflected. In **b**, the periodicity is indicated by coloring one pixel in each unit cell red. The 60° pattern has an actual orientation angle of arctan(7/4) $\approx$ 60.25° and a line spacing of $(12 \times 4)/\sqrt{7^2 + 4^2} \approx 5.95$ pixels, very close to the target values of 60° and 6 pixels. It is horizontally periodic with a period of 12 pixels, and thus allows exact $\pi/3$ phase shifts. (**d**) The action of the ferroelectric SLM as a phase modulator. The electric field direction (i.e. polarization) of the light is shown with red arrows (drawn as if looking toward the SLM) as the light traverses the polarizer cube (Pol, with admission axis shown in green), the half wave plate (HWP, with fast axis orientation shown in blue) and the SLM, for *off* (top row) and *on* (bottom row) pixels. Each pixel of FLC SLM acts as a rotatable half-wave plate: the fast axis (shown here as a blue line) rotates by 45° in *on* pixels relative to *off* pixels. The output electric fields from *off* and *on* pixels have opposite directions, corresponding to the desired relative phase shift by π. The same result could alternatively be achieved without the external half-wave plate if the SLM itself were oriented at a $\pi/8$ angle; the half-wave plate was introduced for convenience. Half of the power is lost in the final polarizing step; the root cause of this inefficiency is that the SLM device was designed for amplitude modulation (in back-projection television) rather than phase modulation, and the loss could be eliminated by using a different FLC material that rotates its retardation axis by 90° instead of 45°.

**Supplementary Figure 3: Function of the rapid polarization rotator**
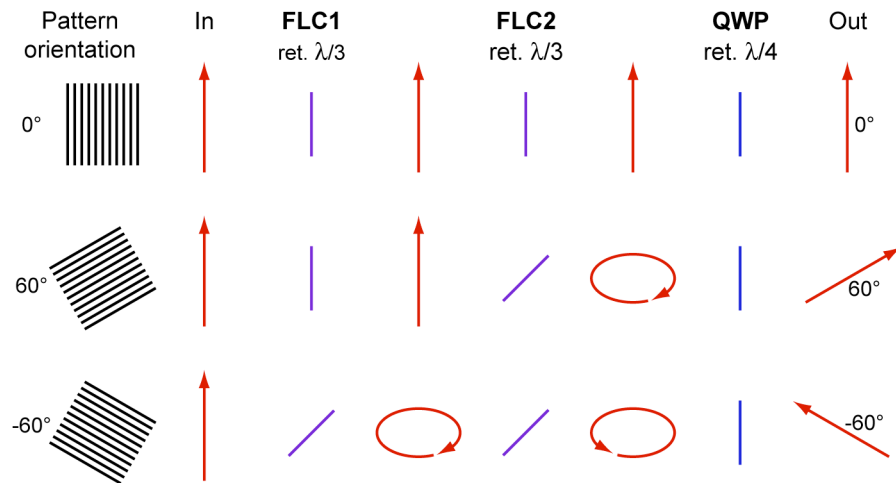
In order to get maximal illumination pattern contrast in the sample at each of the three pattern orientations, the polarization of the light must be correspondingly rotated. This is done by passing the light through a polarization rotator consisting of two identical FLC switchable retarders and a fixed quarter-wave retarder. The two FLC retarders were manufactured with a custom retardance of 1/3 wave. Each of them acts like a 1/3-wave plate whose fast axis orientation can be rapidly (<100 μs) switched from vertical (in the "*off*" state) to 45° (in the "*on*" state) by a digital signal. The red arrows indicate the polarization state of the light as it enters (In), and after traversing each device. Purple and blue bars indicate the fast axis orientation of the liquid crystal retarders (FLC1, FLC2) and the quarter-wave plate (QWP) respectively. When vertical polarization is desired (top row), both FLCs are left unrotated, and the incoming vertical polarization passes through unaltered. To produce a linear polarization at +60° orientation (middle row), only the last FLC device is switched *on*, and to produce a linear polarization at -60° (bottom row), both FLC devices are switched *on*. Ferroelectric liquid crystals were chosen because the more commonly used nematic liquid crystals have switching times >10 ms, which is too slow for this application.

**Supplementary Figure 4:   Beam positions in the pupil plane**
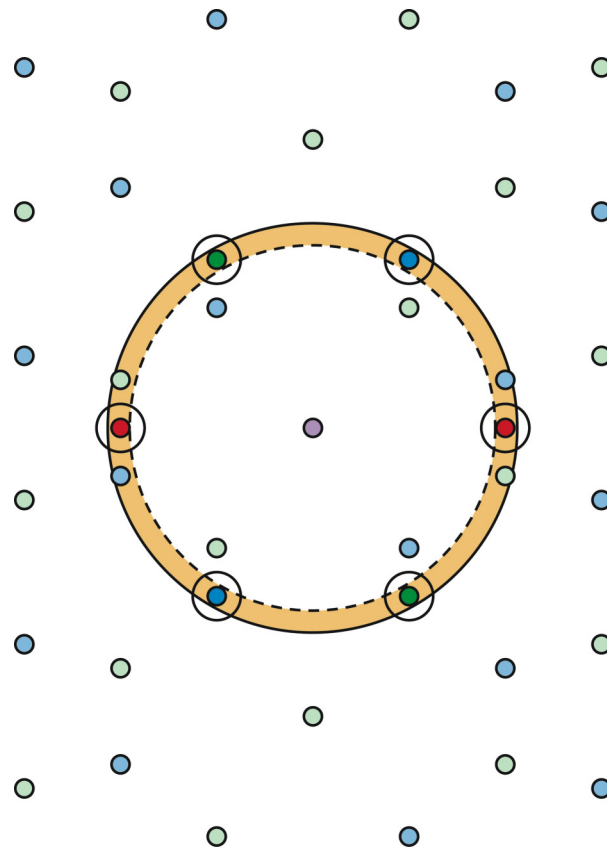
The light beams diffracted off the SLM are focused onto the pupil plane (the objective's back focal plane). The figure shows all possible locations near the pupil plane of diffraction spots caused by the 0° pattern orientation (**Supplementary Fig. 2b**) as red dots, by the 60° pattern (**Supplementary Fig. 2c**) as green dots, and by the -60° pattern as blue dots. (The center order, shown as purple, can be present for all three patterns.) The desired ±1 diffraction orders are shown in dark shades, other "stray" orders in paler shades. The stray orders are caused by our approximating true tilted lines by the pixelated pattern in **Supplementary Fig. 2c**. The TIRF ring, the annular region delimited by the edge of the pupil (large solid circle) and the circle that corresponds to the critical angle for total internal reflection (dashed circle) is shown for reference (tan color). The desired orders all fall well within the TIRF ring. We block the stray orders by placing a fixed mask with six apertures (medium-sized solid circles) in an intermediate pupil plane. The stray orders could alternatively be moved outside the pupil by allocating a larger number of SLM pixels per pattern period, though doing so would either decrease the field of view or require an SLM with more pixels (the current camera and SLM cover ~similar fields of view).

Supplementary Figure 5: Speckles in a stable microtubule that underwent neither polymerization nor depolymerization
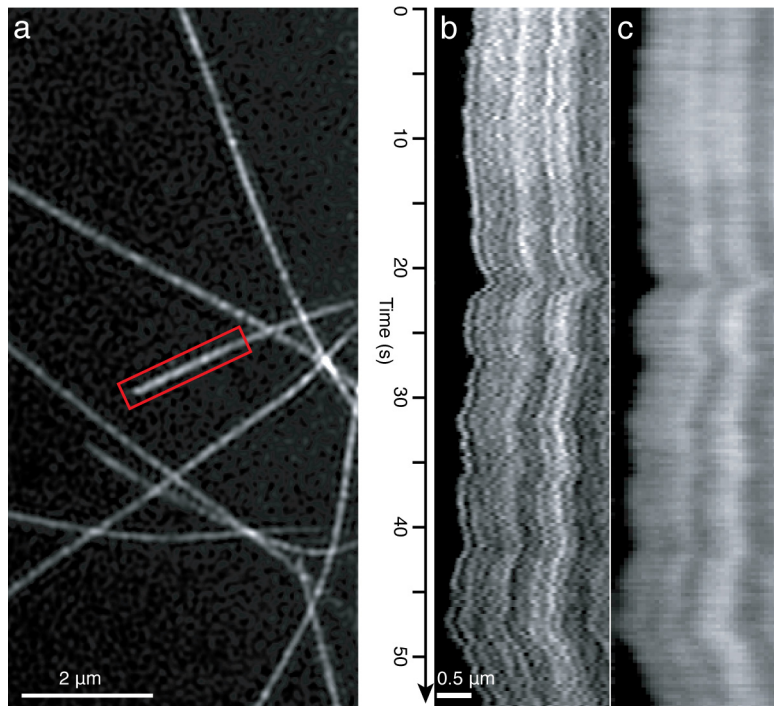

The region indicated by the box in the SIM reconstruction in (**a**) was used to produce SIM (**b**) and conventional (**c**) kymographs. The speckle pattern is seen to persist over time, producing the prominent vertical stripes in the kymographs, and to move in perfect lockstep with the microtubule end. These observations strongly support the conclusion that these patterns represent true variations in labeling density, rather than originating from shot noise (which would be uncorrelated from time point to time point) or from any reconstruction artifact (which would not be expected to follow the microtubule motion).

Supplementary Figure 6: Microtubule flux in a mitotic spindle observed at the single-microtubule level
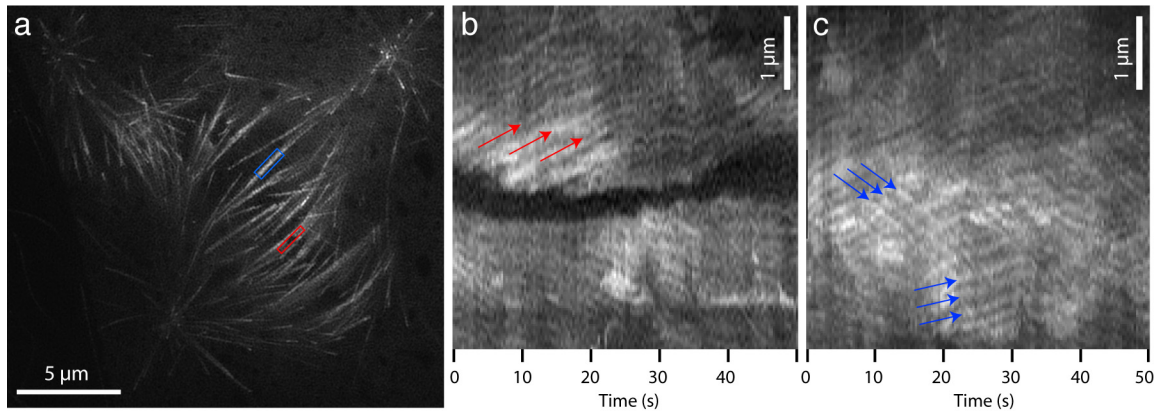
(**a**) One of 200 time frames in a TIRF-SIM time series of a mitotic spindle (which is tripolar because the cell contains three centrosomes, a not uncommon condition in S2 cells[S1]). (**b**) Maximum-intensity kymograph of the area indicated by the red box in (**a**), for 50 one-second time frames. The area includes the nearly-abutting plus ends of two microtubules that originate at different centrosomes. Speckling within each microtubule can be followed over time, and indicates a flux of tubulin towards the centrosome (the microtubule minus end) at a rate of ~1 µm/min (red arrows). Elongation by polymerization at the plus end compensates for the poleward motion. (**c**) Kymograph of the blue-boxed area of (**a**), where microtubules connected to different centrosomes overlap. Moving speckle patterns (blue arrows) indicate that two microtubules move along each other in opposite directions, towards opposite poles. This rapid movement contrasts with the behavior of astral microtubules, which show very little global movement even as they grow and shrink rapidly by polymerizing or depolymerizing at their plus end (compare **Fig. 2c** of the main text).

Supplementary Figure 7: Motion artifacts when live SIM is attempted at insufficient acquisition speed
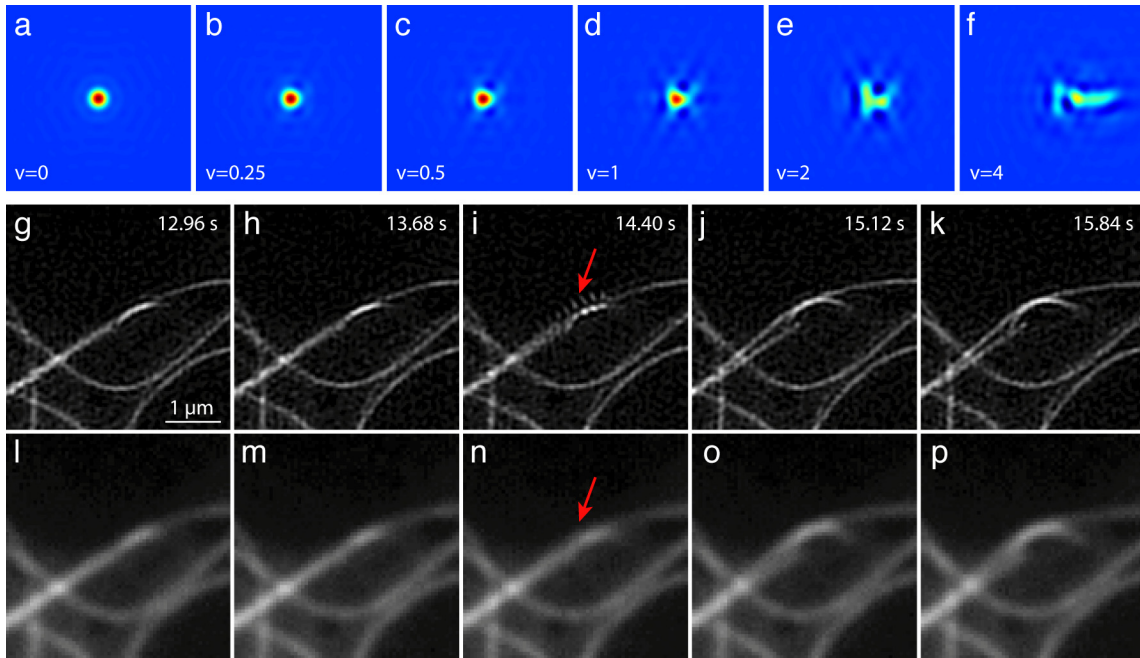
a–f: Reconstructions from a SIM simulation of a point-like object that moves during data acquisition, with a velocity of 0, 0.25, 0.5, 1, 2, or 4 times the SIM resolution distance per time point. (In this simulation the SIM resolution was 84 nm; the field of view shown here is 1.23 μm.) The object is located in the center of the field when acquisition starts, and moves rightward. The figure should be understood to illustrate only the magnitude of the distortion, not its precise shape, as the latter depends on the direction of motion relative to the pattern shift directions, starting position relative to first pattern, any acceleration, etc.

g–p: Consecutive SIM reconstructions (**g–k**) and corresponding conventional images (**l–p**) of EGFP-α-tubulin in S2 cells, from a relatively slow time series acquired with 80 ms exposure times (i.e. 720 ms per SIM sequence). The red arrows indicate a microtubule pair that appears to suddenly snap loose after having been stuck. The snapping motion occurred during acquisition of the time point shown in panels **i** and **n**, and was fast compared to the acquisition time of the 9-image sequence used for one SIM time point (it was completed in <2 raw images). This rapid change caused an obvious artifact in the reconstruction of frame **i** (arrow). To avoid this type of artifact, the time to acquire one SIM time point should be short compared to the time scale of relevant sample motions.

For slow movements, the residual motion artifacts can in principle be prevented entirely (except for the first and last time point) by computationally synchronizing the 9 raw images that constitute each time point. This would be done by multiplying the temporal Fourier transform of the image sequence for each pattern phase by a phase gradient corresponding to the time delay of acquiring that phase within each 9-image sequence. This process is justified if the image sequence for a given phase is oversampled temporally in the Nyquist sense, which is true if no movement exceeds ~half the SIM resolution distance per time point.

Supplementary Note: 3D super-resolution microscopy

This article mainly discusses two-dimensional microscopy. Several existing methods have achieved super-resolution light microscopy also in three dimensions, on static samples. For example, STED can be optimized for either axial[S2] or lateral resolution[S3] by choosing a suitable STED beam shape, and high 3D resolution can be achieved by combining both beam types incoherently[S4]. Three-dimensional versions of the localization-based super-resolution microscopies PALM, STORM and FPALM have been published[S5–S7]. Both for STED and for PALM, the greatest axial resolution was achieved by exploiting interferometric effects in a geometry where the specimen is located between two opposing objective lenses (forming isoSTED[S8] and iPALM[S9] respectively).

SIM has also been done in 3D, either through a single objective lens [20,S9], or, for greater axial resolution, by using two opposing objective lenses interferometrically[S10] (I^5S). The practical implementations have been slow, and limited so far to static samples. The hardware used here for 2D TIRF-SIM could also be used for 3D SIM with only minor modifications:
- 3D SIM typically uses three beams, formed by diffraction as the -1, 0 and +1 diffraction orders from a grating[20], whereas the 2D SIM used here only makes use of the ±1 orders. Therefore the SLM patterns would need to be modified slightly, to produce three diffraction orders of comparable intensity. The more complex interference pattern formed by the three beams also requires images at five different pattern phases for separation of the sample information components, whereas three phases suffice for 2D SIM. To allow 5 equally-spaced phases, the SLM pattern should have a horizontal or vertical periodicity that is a multiple of 5 pixels, instead of a multiple of 3 pixels as required for 2D SIM. A simple choice would be to discard one pixel from each horizontal period of the pattern in **Supplementary Fig. 2b**, and two pixels from each horizontal period of the pattern in **Supplementary Fig. 2c**. In other words, the resulting 60° pattern would have a unit cell defined by the vectors (7,4) and (10,0), rather than (7,4) and (12,0) as in **Supplementary Fig. 2c**; because the unchanged vector (7,4) defines the pattern tilt angle, which in turn determines the ratio of the pattern period to the ideal one, these parameters would remain near-ideal approximations. The relative intensity of the zero and ±1 orders can be coarsely adjusted by choosing the number of *on* pixels in each horizontal period, and fine-tuned by rotating the half-wave plate (see **Supplementary Fig. 1–2**).
- The pupil-plane beam block would need to be modified, and in particular given a center hole to admit the zero-order beam.
- The demagnification factor from the SLM to the sample may need to be changed, to place the beams at an appropriate radial position (typically 90–95% of the pupil radius) within the back focal plane of the chosen objective lens (preferably a high-NA water immersion lens).

Live 3D SIM would require a larger number of raw images per time frame than in 2D, for two reasons:
- It would use 15 instead of 9 raw images per axial plane (five phases at each of three orientations[20]).
- At each time point it would use a focal series of axial planes spaced about 150 nm apart.

The larger number of images would lead to a slower frame rate, for a given camera read-out rate. The maximum rate of sample motion that could be tolerated would thus decrease, in proportion to the sample thickness. The technique would be quite feasible on relatively thin samples, however, if sample movement speeds are modest. For example, using similar imaging speed and number of raw exposures as was used here for 2D imaging, a 1-µm-thick volume could be observed by SIM at a ~1 Hz rate, with ~100 x 100 x 300 nm 3D resolution, for about 40 time points.

Supplementary References

S1. Gergely, F. and Basto. R. *Genes & Dev.* **22**, 2291-2296 (2008).

S2. Willig, K.I., Rizzoli, S.O., Westphal, V., Jahn, R. & Hell, S.W. *Nature* **440**, 935–939 (2006).

S3. Klar, T.A., Jakobs, S., Dyba, M., Egner, A. & Hell, S.W. *Proc. Natl. Acad. Sci. USA* **97**, 8206–8210 (2000).

S4. Harke, B., Ullal, C.K., Keller, J. & Hell, S.W. *Nano Letters* **8**, 1309–1313 (2008).

S5. Shtengel, G. *et al.*, *Proc. Nat. Acad. Sci. USA*, **106**, 3125–3130 (2009).

S6. Huang, B., Wang, W., Bates, M. & Zhuang, X. *Science* **319** 810–813 (2008).

S7. Juette, M.F., Gould, T.J., Lessard, M.D., Mlodzianoski M.J., Nagpure, B.S., Bennett, B.T., Hess, S.T. & Bewersdorf, J. *Nat. Methods* **5**, 527–529 (2008).

S8. R. Schmidt, R., Wurm, C.A., Jakobs, S., Engelhardt, J., Egner, A., & Hell, S.W. *Nat. Methods* **5**, 539–544 (2008).

S9. Schermelleh, L., Carlton, P., Haase, S., Shao, L., Winoto, L., Kner, P., Burke, B., Cardoso, M.C., Agard, D.A., Gustafsson, M.G.L., Leonhardt, H. & Sedat, J. W. *Science* **320**, 1332-1336 (2008).

S10. Shao, L., Isaac, B., Uzawa, S., Agard, D.A. & Sedat, J.W. *Biophys. J.* **94**, 4971–4983 (2008).